

RANS Based Numerical Simulation of Horizontal Axis Wind Turbine

Liu Su ^a, Isam Janajreh ^{a*}

^a Department of Mechanical Engineering, Khalifa University, Abu Dhabi, UAE

Abstract

A three-dimensional (3D) Computational Fluid Dynamics (CFD) model has been developed in this work to study 3.5kW Horizontal Axis Wind Turbine (HAWT). The model is based on the incompressible Navier-Stokes flow that accounts for the turbulence via SST $k-\omega$ turbulence model in a Single Rotating Reference Frame (SRF) that considers the rotor rotation. A body-fitted multi-block mesh is constructed around the turbine rotor with high-resolution mesh in the high-velocity gradient regions and in conjunction with the standard law of the wall next to the blade surface. The model comprises 4.5 million hexahedral elements; the blade is specifically wrapped in an O-grid boundary layer to achieve the desirable y^+ value (<60). The flow around the blade was studied in detail (velocity, pressure, etc.) and results of the power coefficients were compared to the experimental data, which showed a plausible trend. The developed procedures can be easily and economically applied to any given HAWT configuration making the CFD a virtual wind tunnel in another complex atmospheric boundary layer flow. In view of these results, 2D blade mode is also developed and the power coefficient (C_p) values for the two models are compared. The results emphasized the role of rotation and radial momentum and demonstrated large discrepancies in the attained blade pressure values.

Keywords: CFD, HAWT, SRF, SST $k-\omega$, Wall modeling

1. Introduction

Onshore annual wind energy potential was estimated to be 96 PWh [1], representing 7 times the total electricity consumption in 2001. The enormous interest in wind energy lead to over 30% annual growth in 2012 reaching nearly 300GW global implementation and the development of wind atlas by the Global Wind Energy Council [2].

Today, industrial design codes for wind turbines are still based on Blade Element Momentum (BEM) method because of its simplicity and the reasonable accuracy it offers. Detailed implementation of the method and the different imposed corrections can be found in the current authors' previous work [3]. BEM method, however, fails to provide a detailed picture of the rotating flow field, its separation and reattachment regions, turbulence, and their combined effects [4]. The rotational effect may result in phenomena like stall-delay, lift

augmentation, spanwise flow, and thus is crucial for accessing the wind turbine power generation and aeroelastic predictions. Lifting line surface theory is another approach to resolving the flow field of HAWT. It is based on the unsteady vortex lattice method that solves the potential flow field. Implementation of this method on flapping wind flight is found in Ghommem's work [5].

Computational Fluid Dynamics (CFD) draws much attention recently as computational power and memory storage made a leap frog in the last few years. Generalized Actuator Disc Model based on complete Navier-Stokes equations has been implemented to analyze the wind turbine rotor performance, which demonstrated good results in axisymmetric flow conditions by comparing with experimental results [6-9]. As the CFD solvers are capable of handling viscous flow on rotors, their applications to wind turbines are of practical interest.

Turbulence is the natural state of the flow over the wind turbine. A review of this subject and the different models and their computational cost can also be found in the previous work of the

* Corresponding author. Tel.: +1234567890

Fax: +9876543210; E-mail: Author.Name@iasks.org

© 2016 International Association for Sharing Knowledge and Sustainability

DOI: 10.5383/ijtee.18.02.001

authors [3] per Fig. 1. A summary is given here due to its importance. Generally, the time-averaging of the dependent variable $\bar{\phi}$, e.g., velocity, pressure, density, etc., over a time t_1 interval is given by:

$$\bar{\phi} = \frac{1}{t_1} \int_{t_0}^{t_0+t_1} \phi dt \quad (1)$$

The CFD model is based on the fundamental mass and momentum (and energy in the case of compressible or non-isothermal flow) conservation laws. Therefore, the time-averaged Navier-Stokes equations, which are referred to as RANS equations, are written as:

$$\text{Conservation of mass: } \frac{\partial \rho}{\partial t} + \frac{\partial \rho U_i}{\partial x_i} = 0 \quad (2)$$

$$\begin{aligned} \text{Conservation of momentum: } & \frac{\partial \rho U_i}{\partial t} + \frac{\partial \rho U_j U_i}{\partial x_j} \\ & = \frac{\partial}{\partial x_j} \left(\mu \frac{\partial U_i}{\partial x_j} - \rho \overline{u'_i u'_j} \right) - \frac{\partial P}{\partial x_i} + F_i \end{aligned} \quad (3)$$

Where ρ is the density, U_i is the time-averaging of the i -component velocity, u'_i is the fluctuations in the i -component velocity, μ is molecular viscosity, P is the static pressure and F_i are body forces. The term $-\rho \overline{u'_i u'_j}$ is known as Reynolds Stresses and lends the enclosure to the system. The Boussinesq approach relates the Reynolds stresses to the mean flow by a turbulent/eddy viscosity, μ_t , as shown below:

$$-\rho \overline{u'_i u'_j} = 2\mu_t S_{ij} - \frac{2}{3}\mu_t \frac{\partial U_k}{\partial x_k} \delta_{ij} - \frac{2}{3}\rho k \delta_{ij} \quad (4)$$

Where $S_{ij} = \frac{1}{2} \left(\frac{\partial U_i}{\partial x_j} + \frac{\partial U_j}{\partial x_i} \right)$, k is the turbulent kinetic energy and δ_{ij} is the Kronecker delta. It is noted that the μ_t is flow property instead of fluid property. The problem now lies in obtaining means or models to find the new two unknowns (k and μ_t). Different models are proposed, including zero equation model (e.g., Algebraic Model), one transport equation model (e.g., Spalart-Allmaras model), two transport equation model (e.g., k - ω model, and k - ϵ model). These models, as we commonly refer to, are first-order models. The first order turbulence model deals with isotropy of turbulence and 2nd order modeling overcomes this issue. The most famous 2nd order models are the Algebraic Stress Model (ASM) and the Reynolds Stress Model (RSM). Fig. 1 illustrated different turbulence models and their computation cost, as shown below.

The k - ω turbulence models are undoubtedly the most common models, especially in wind energy applications. In the k - ω turbulence models, the transport equation of the turbulent kinetic energy is solved together with the equation of the specific rate of dissipation of turbulent kinetic energy (ϵ), and is defined as $\epsilon = k/\omega$. This model performs well in free shear flows, flat plate boundary layer flows, complicated adverse pressure gradient flows, and separated flows. A problem of the standard k - ω model is the dependency on the free stream boundary conditions. The SST k - ω model is similar to the standard k - ω model but includes a number of features that make the SST k - ω model more robust for a wider class of flows (e.g., adverse pressure gradient flows, airfoil, and transonic shock waves) than the standard k - ω model. The SST k - ω model equations are given [10] and are written as:

$$\frac{\partial}{\partial t} (\rho k) + \frac{\partial}{\partial x_i} (\rho k u_i) = \frac{\partial}{\partial x_j} \left(\Gamma_k \frac{\partial k}{\partial x_j} \right) + \overline{G}_k - Y_k + S_k \quad (5)$$

$$\begin{aligned} \frac{\partial}{\partial t} (\rho \omega) + \frac{\partial}{\partial x_i} (\rho \omega u_i) &= \frac{\partial}{\partial x_j} \left(\Gamma_\omega \frac{\partial \omega}{\partial x_j} \right) + G_\omega - Y_\omega + D_\omega \\ &+ S_\omega \end{aligned} \quad (6)$$

Where \overline{G}_k represents the generation of turbulence kinetic energy due to mean velocity gradients, G_ω represents the generation of ω . The Γ_k and Γ_ω represent the effective diffusivity of k and ω , respectively. The Y_k and Y_ω represent the dissipation of k and ω due to turbulence, D_ω represents the cross-diffusion term, S_k and S_ω are user-defined source terms [11]. In turbulence flow, it is of extreme importance to model the flow close to the wall without excessive computational cost. Successful prediction of frictional drag for external flow depends on the high fidelity of local wall shear predictions. Therefore, using a very fine mesh to resolve the steep profiles is still too expensive for many industrial CFD simulations particularly for unsteady cases such as rotating turbine rotor. In turbulent flow, near-wall region is divided into three layers: the laminar viscous sub-layer, the transitional buffer layer, and the fully turbulent layer. Over a no-slip wall at a high Reynolds number, it is more economical to use the semi-empirical Wall Function (WF) than directly solving a fine wall mesh. Near-wall models aim to resolve the flow right up to the boundary, which strictly requires the near-wall grid node to satisfy $y^+ \leq 1$, where y^+ is the non-dimensional normal wall distance defined by:

$$y^+ = \frac{u_\tau y}{\nu} \quad (7)$$

where u_τ is the wall velocity and is equal to $\sqrt{\tau_\omega/\rho}$, τ_ω is the wall shear stress, y is the height of the first cell, ν is the kinematic viscosity. The demanding requirement for the grid resolution makes the computation extremely expensive, particularly for the high Reynolds number flows. In wall functions, each wall-adjacent cell's centroid is recommended to be located within the log-law layer, where $30 \leq y^+ \leq 300$. A value close to the lower bound ($y^+ \sim 30$) is most desirable. As much as possible, the mesh should be made either coarse or fine enough to prevent the wall-adjacent cells from being placed in the buffer layer ($5 \leq y^+ \leq 30$). In this work, care was taken targeting $y^+ \sim 50$ value and is iteratively verified by using equation (7).

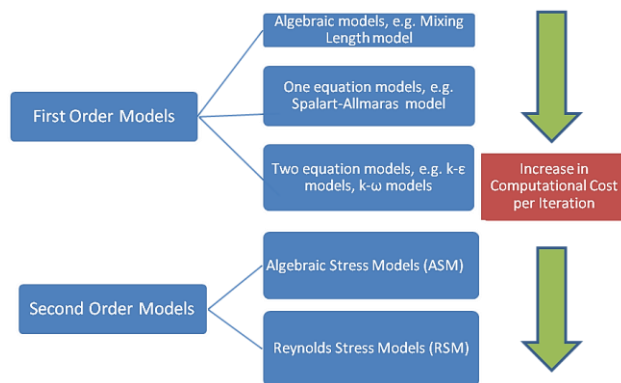


Fig. 1. Different turbulence models and their computation cost

2. Numerical Model

The numerical model is a 120-degree wedge built around the 3.5kW, 3 bladed, 4m rotor diameter, HAWT. The blades show a slight twist along their spans to accommodate the increasing rotor radius. The blades have a rounded tip with an airfoil shape similar (but not exactly) to S809. Neither the tower nor the ground is included in the model, and a uniform wind speed profile at 10% turbulence intensity is imposed at the entrance of the domain to accommodate the atmospheric boundary layer turbulence. The computation domain is cylindrical shaped at 4 blade spans in the radial direction and extending 6.25, and 16.25 blade lengths upstream and downstream, respectively. The whole computation domain is depicted in Fig. 2 which consists of inner and outer domains to simplify the meshing.

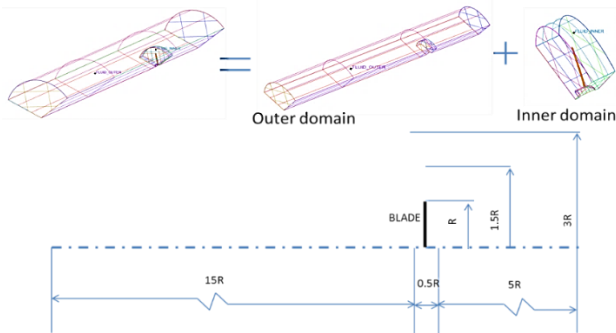


Fig. 2. Description of the computation domain

The domain is carefully padded and discretized into hexahedral cells using ICEM to account for the boundary layer mesh (reasonable aspect ratio, low twist, and warp angles). Hexahedral mesh type produces fewer elements and nodes to the tetra type mesh for the same computational domain and consequently saves in memory, storage, and time to compute the solution [12]. The solid geometry was initially constructed in an AutoCAD environment and transferred as IGES file into ICEM. The mesh comprises approximately 4.5 million hexahedral cells. Due to the geometrical complexity of the blade particularly near the blade root and the blunt blade tip multi-block strategy is adapted which greatly facilitated the meshing. Initially, the whole domain is fitted with a single block and is subdivided into as many as 120 blocks to enable hexahedral meshing, as shown in Fig. 3. Three O-grids are built around the blade in order to obtain the desired local resolution, as detailed in Fig. 4.

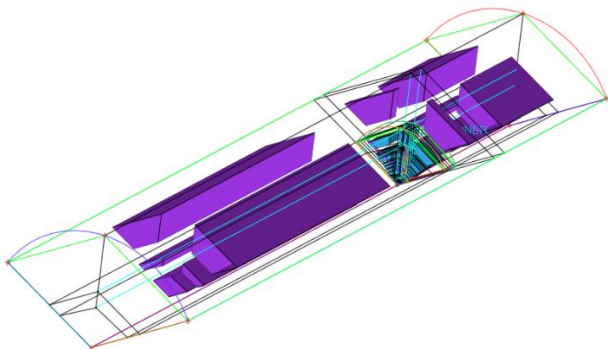


Fig. 3. Ultimate blocks for the whole domain

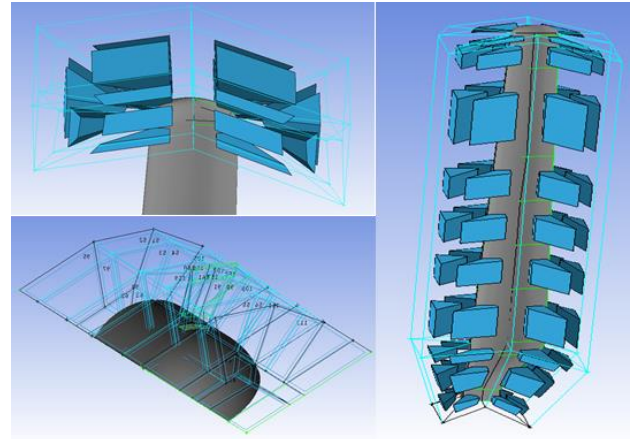


Fig. 4. O-grids around the blade, blade root, and tip

The 120 degrees domain takes the form of a wedge. It encloses one of the three HAWT rotor blades and hence periodic boundary condition is applied at the two rotating faces of the wedge. Nonconformal mesh is utilized to reduce the number of cells in the outer domain region, as shown in Fig. 5. The mesh count is summarized in Table 1.

Table 1: Mesh details for the whole domain

Domain	Mesh type	Element count	Height of first row (m)	Inflation ratio	Number of rows
Inner domain	Hexahedral	3.4 million	-	-	-
Outer domain	Hexahedral	1.1 million	-	-	-
Around the blade	Hexahedral	-	0.0001	1.2	8

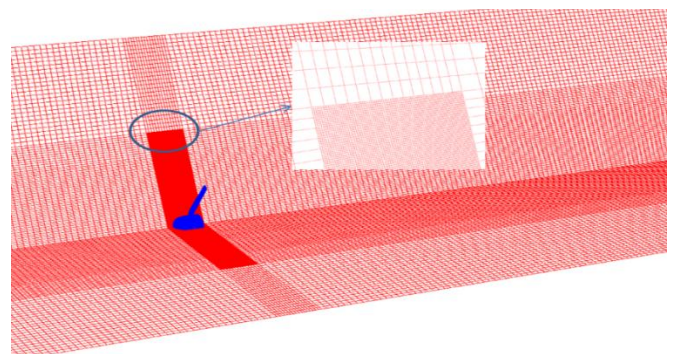


Fig. 5. Non-conformal mesh between the inner and outer domains

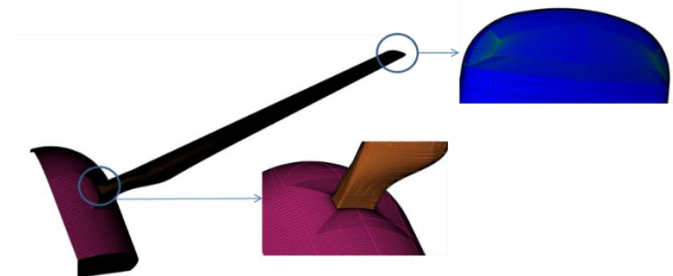


Fig. 6. Mesh around the blade

The mesh around the blade is shown in Fig. 6. The faces and domains are labeled, as shown in Fig. 7 and their assigned boundary conditions are summarized in Table 2.

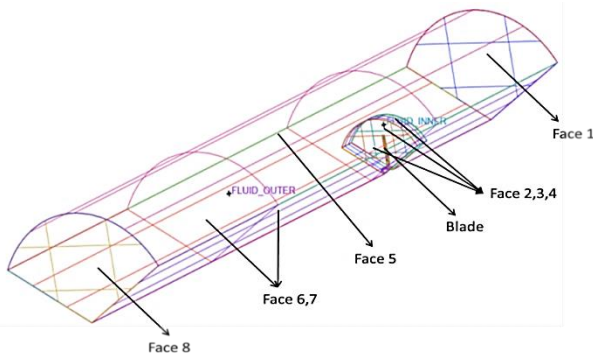


Fig. 7. Labeled faces and domains, face 1 upstream (z=0), and face 8 is downstream

Table 2: Boundary condition assignment

Face 1	Velocity inlet (u = v = 0, w = constant)
Face 2, 3, 4	Interface
Blade	No-slip wall
Face 5	Symmetry
Face 6, 7	Periodic
Face 8	Outflow

The inner core of the fluid materials that houses the blades is specified as a single rotating reference frame model (SRF); this lends the problem in seeking a steady-state solution. Sliding mesh can also be sought at a higher computational cost as it is inherently transient [10]. In the current study, the steady and pressure-based solver of ANSYS Fluent [10] is used which is based on the SIMPLE pressure-velocity coupling scheme and following a 2nd order upwind spatial discretization scheme. The convergence criterion is set at 10⁻⁵ for the continuity and the three (u, v, and w) momentums as well as for the turbulence k and ω equations.

2.1. Mesh independence study

Assessment of the mesh solution dependency is carried out through four levels of meshes: Fine, baseline, course I, and course II, and comprising 5.5, 4.5, 3.05, 2.26 million cells, respectively. Results of the thrust and torque under the same boundary conditions (i.e., 5m/s velocity inlet, zero rotation speed, and zero velocity gradient at the outlet) are listed in Table 3.

Table 3: Mesh sensitivity on the computed thrust and torque

Level	Size (cells) x10 ⁶	Thrust (N)				Torque (N.m)			
		Pressure based	Err. (%)	Viscous based	Err. (%)	Pressure based	Err. (%)	Viscous based	Err. (%)
Refined	5.5	33.62	--	0.16	--	5.97	--	0.03	--
Baseline	4.5	33.95	0.98	0.16	0.00	6	0.50	0.03	0.00
Coarse I	3.05	34.37	2.23	0.155	3.13	5.86	1.84	0.024	20.00
Coarse II	2.26	34.68	3.15	0.15	6.25	5.75	3.69	0.02	33.33

The pressure and the viscous-based prediction are within acceptable values for the thrust and torque. The relative error in

the thrust and torque attributed to the pressure- and viscous-based is below 1% in the baseline mesh.

3. Results and Discussion

3.1. Experimental validation

Measurements of the power generations under different wind speeds for the 3.5kW HAWT were carried out by Centro de Investigaciones Energéticas, Medioambientales Tecnológicas (CIEMAT) [13]. The generated power was recorded simultaneously with the rotational velocity with sweeping values for the incoming velocity, thereby allowing evaluating the influence of tip speed ratio (TSR). Their computed torque and thrust data were compared to the corresponding simulated values as tabulated in Table 4 and presented in Fig. 8. Furthermore, the inferred experimental measurements of power coefficient ($C_p = \omega \times T / (0.5 \times u^3 \times A)$) and simulation results are depicted in Fig. 8. A good agreement between the CFD simulation and experimental data is shown, particularly up to 8m/s incoming velocity. The discrepancy beyond 8m/s velocity is mainly due to the change of the angle of attack activated through the “Blade Pitching Mechanism” used in the actual turbine system. The trend has been captured experimentally as reducing the angle of attack leads to a reduction in the power coefficient. Discrepancies are also traced back to rotational effect and turbulence modeling, as the wind speed increases separation and stall of the flow occurs over the blade that limits the SST k-ω turbulence model and the adopted steady approach of SRF in capturing the accurate flow physics.

Table 4: Torque and thrust obtained at various wind speeds

Run #	Wind speed (m/s)	Rotational speed (rad/s)	TSR (-)	Torque (N.m)	Thrust (N)
1	3	9.5	6.41	2.07	24.53
2	4	12.5	6.33	3.83	41.86
3	5	13.5	5.47	8.72	51.03
4	6	14.73	4.97	12.65	75.34
5	7	16.47	4.76	17.89	98.46
6	8	18.58	4.70	23.77	127.16
7	9	20.85	4.69	32.91	165.97
8	10	23.26	4.71	37.75	199.86
9	11	25.98	4.78	45.62	246.15
10	12	28.55	4.82	54.50	295.92
11	13	30.06	4.68	65.02	337.48

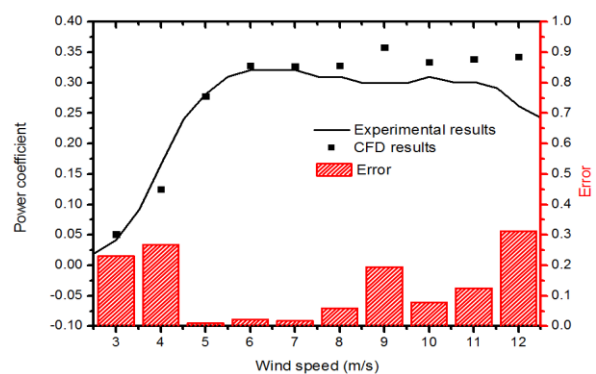


Fig. 8. Comparison of power coefficients vs wind speed

3.2. Flow field study

The authors' previous work illustrated the role of the tip speed ratio [3]. In the absence of fluid structural coupling, they emphasized on the discrepancy between the tip speed ratio and incurred torque. This situation occurs during a mismatch between incoming wind speed and wind turbine rotation. The difference in the achieved power coefficients can reach as high as 60 times between less favored and optimal TSR values and hence a wise choice of the TSR is necessary.

In order to make full use of CFD simulation, a detailed analysis of the flow field is conducted. All the flow field results in this section were based on the case of 5m/s velocity inlet and 12rad/s rotational speed. The streamlines on the blade (both pressure and suction side) are plotted in Fig. 9. Fig. 10 shows the pathlines of the flow over the blade (colored by velocity magnitude). One can notice the radial tendency of the flow particularly in the higher velocity suction side as well as the increase in the velocity magnitude starting the low velocity in the root region and ending at high velocity towards the tip.

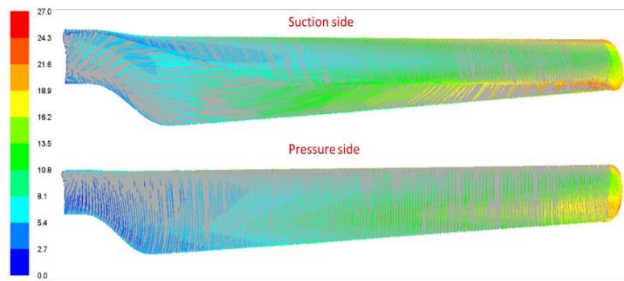


Fig. 9. Streamlines on blade under 5m/s velocity inlet and 12rad/s rotational speed colored with velocity magnitude

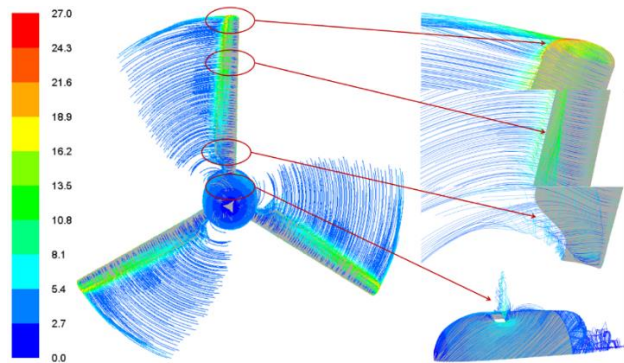


Fig. 10. Path lines over blade under 5m/s velocity inlet and 12rad/s rotational speed colored with velocity magnitude

Fig. 11 shows the velocity magnitude and static pressure plots at several radial locations, 20%, 40%, 60%, and 80% of blade length. The maximum velocity magnitude and static pressure increases as the flow reaches a further radial distance. As the section of the airfoil is located at a longer radius subjected to an optimal angle of attack, it contributes more to the generation of power. Fig. 12 shows the radial and axial velocity magnitude plots at the same radial locations. High radial velocity can be observed at positions closer to the rotation axis, while higher axial velocity is observed at positions further to the rotation axis. The vorticity and turbulence intensity along the blade was plotted in Fig. 13. In the vorticity plot, the blue color that almost fills the entire slice represents the potential field past the blade; the boundary layer, however, is clearly visible as a thin, red-

oriented belt around the airfoil sections. The plot vividly shows the flow behavior along the blade spanwise: as one moves radially from the rotational axis, the angle of attack decreases, as the high vorticity belt appears to be thinner. A similar phenomenon can also be observed in the turbulence intensity plot.

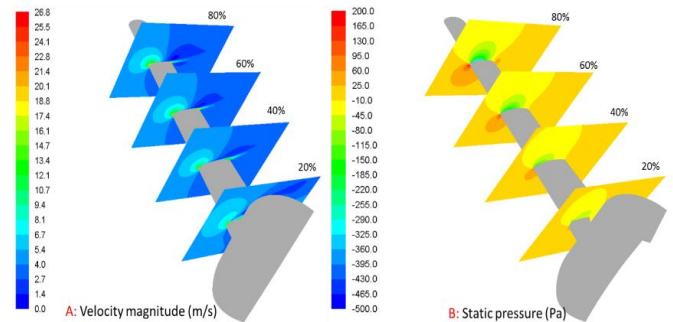


Fig. 11. Velocity magnitude and static pressure slice plots

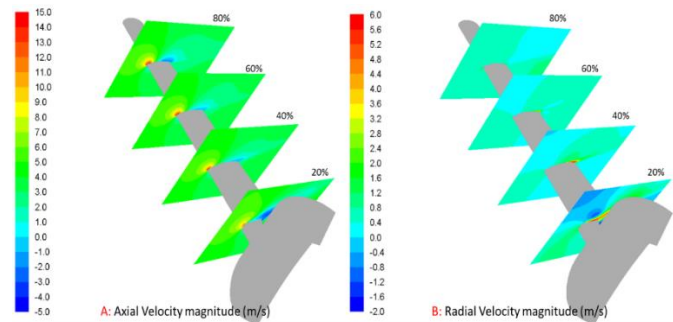


Fig. 12. Velocity magnitude and static pressure slice plots

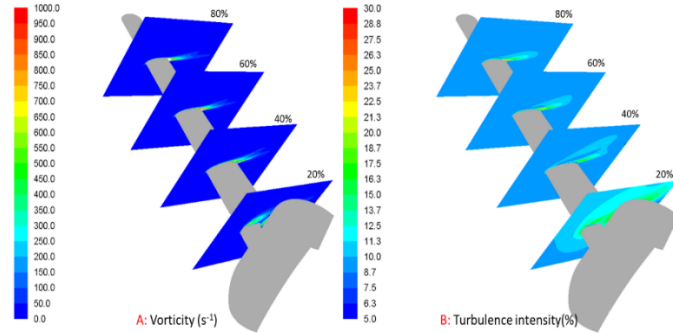


Fig. 13. Vorticity and turbulence intensity plots along the blade

3.3. Rotational effects study

As indicated by the author's previous study [3], the rotation has a significant impact on the wind turbine power generation and pertains to the most challenge to be factored in Blade Element Momentum (BEM) method. In the current study, the rotational effects are studied by plotting pressure coefficients distribution on the blade at different radii, as shown in Fig. 14 through 16.

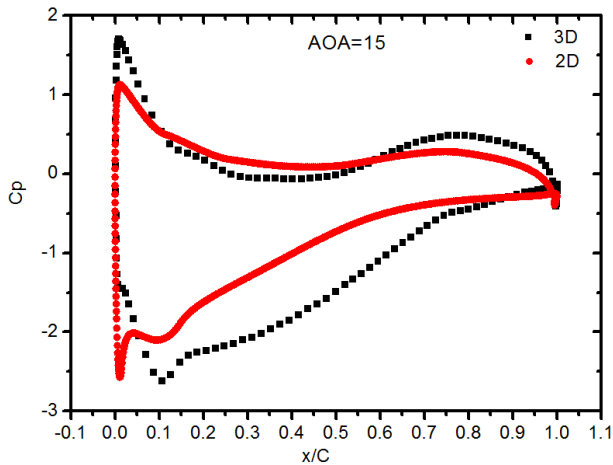


Fig. 14. Pressure coefficients distribution along the airfoil for both 3D and 2D flow condition when angle of attack (AOA) is 15 degrees ($r/R=78.1\%$)

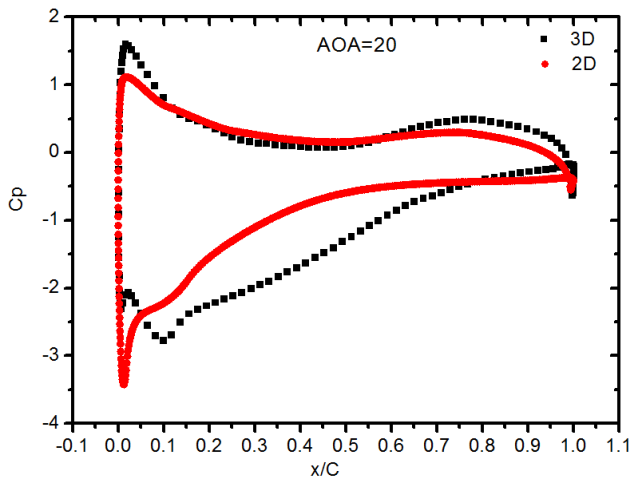


Fig. 15. Pressure coefficients distribution along the airfoil for both 3D and 2D flow condition when angle of attack (AOA) is 20 degrees ($r/R=57.5\%$)

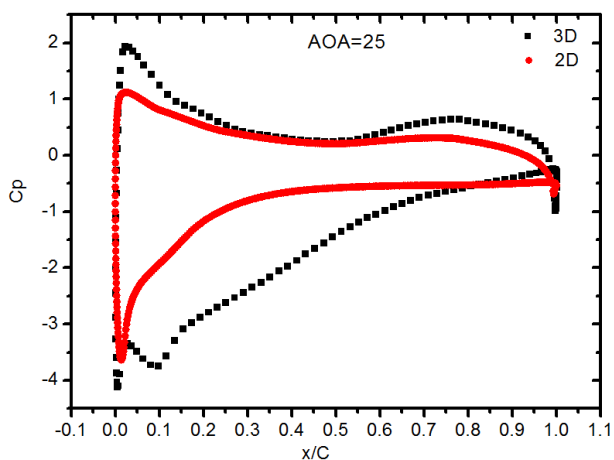


Fig. 16. Pressure coefficients distribution along the airfoil for both 3D and 2D flow conditions when the angle of attack (AOA) is 25 degrees ($r/R=44.9\%$)

Three cases were inferred for a detailed study of the pressure coefficient at a matching angle of attack (AOA) between the 2D cases and 3D cases. The 3D cases are matched by taking the blade section at the corresponding radial distances, i.e., at 78.1%, 57.5%, and 44.9% blade length that corresponds to 15, 20, and 25 degrees AOA. In the determination of the 3D angle of attack, the angle between the incoming wind speed vector and rotational speed vector of the wind turbine is inferred considering near-zero pitch and twist angles. The superimposition of the C_p sectional profiles shows that 2D and 3D follow similar trends. There are, however, two distinct discrepancies: First, the 3D is observed to produce a lower pressure in the suction region. This is due to the promotion of the radial momentum in particular in the suction blade side that leads to lower pressure in which the 2D case fails to produce. Therefore, any attempt based on BEM must be adjusted to the blade rotational effect as such discrepancy is attributed to lack of rotational effect. Second, the extreme values for negative pressure (stagnation point) are more pronounced in the 3D case. This is attributed to the level of turbulence which increases the localize flow momentum and based on energy conservation resulted in higher stagnation pressure. The uniqueness of the negative pressure peak in the 3D cases is their slow development when compared to the 2D cases. Therefore, there is a delay in their appearance that moves toward the trailing edge in the 3D cases. It is also noticed that the suction side pressure increases smoothly in the 3D cases compared to the abrupt increase in the 2D case. With these observations in mind and integrating the pressure/suction area, there is no doubt that 3D cases resulted in higher lift/torque than the 2D cases. Such phenomenon was also observed and emphasized in Carcangu's work[14].

4. Conclusion

A 3D high fidelity CFD study for full scale three-bladed 3.5kW HAWT turbine is carried out. The model is based on the full Navier-Stokes equation and SST $k-\omega$ RANS turbulence. In order to reduce the computation effort, one-third of the rotor domain was modeled enclosing one turbine blade and the periodic boundary condition was imposed. The model was meshed in ICEM using 120 blocks and comprises 4.5 million hexahedral elements. The forces on blades were first reported under different operation conditions and based on which the power coefficients were obtained. The obtained power coefficients from CFD simulation are in agreement with the reported experimental data, particularly under low wind speed, e.g., $<9\text{m/s}$ before triggering of the centrifugal pitching mechanisms and prior to the massive separation that risk the efficiency of the SST $k-\omega$ turbulent model. The developed procedures can be easily and economically applied to any given HAWT configuration avoiding the complexity of atmospheric boundary layer wind tunnel testing and advocating CFD as the current virtual wind tunnel. Further analysis on the flow field was conducted to have a deeper insight at the flow past the rotational HAWT. The results showed the flow behavior past the blade and emphasized the influence of the rotation on pressure distribution along the blade.

Acknowledgments

The financial support received from Khalifa University and the generous sponsorship and data support of the Sonkyo Energy team (Iñigo Portillo, Christophe Lopez, Javier Vidal, and José Luis) is highly acknowledged.

References

- [1] R. McKenna *et al.*, “High-resolution large-scale onshore wind energy assessments: A review of potential definitions, methodologies and future research needs,” *Renew. Energy*, vol. 182, pp. 659–684, 2022, doi: 10.1016/j.renene.2021.10.027.
- [2] J. Lee and F. Zhao, “Global Wind Report 2021,” *Glob. Wind Energy Council*, pp. 1–80, 2021, [Online]. Available: <http://www.gwec.net/global-figures/wind-energy-global-status/>.
- [3] S. Liu and I. Janajreh, “Development and application of an improved blade element momentum method model on horizontal axis wind turbines,” *Int. J. Energy Environ. Eng.*, vol. 3, no. 1, pp. 1–10, 2012, doi: 10.1186/2251-6832-3-30.
- [4] C. Lindenburg, “Investigation into Rotor Blade Aerodynamics Analysis of the stationary measurements on the UAE phase-VI rotor in the NASA-Ames wind tunnel,” *Ecnnl*, no. July, p. 114, 2003, [Online]. Available: <http://www.ecn.nl/docs/library/report/2003/c03025.pdf>.
- [5] M. Ghommem, “Modeling and Analysis for Optimization of Unsteady Aeroelastic Systems,” pp. 1–192, 2011, [Online]. Available: <http://scholar.lib.vt.edu/theses/available/etd-11152011-193632/>.
- [6] H. Daaou Nedjari, O. Guerri, and M. Saighi, “Full rotor modelling and generalized actuator disc for wind turbine wake investigation,” *Energy Reports*, vol. 6, pp. 232–255, Feb. 2020, doi: 10.1016/j.egy.2019.10.041.
- [7] J. Cao, W. Zhu, W. Shen, J. N. Sørensen, and T. Wang, “Development of a CFD-based wind turbine rotor optimization tool in considering wake effects,” *Appl. Sci.*, vol. 8, no. 7, 2018, doi: 10.3390/app8071056.
- [8] E. Mahmoodi, A. Jafari, and A. Keyhani, “Wind turbine rotor simulation via CFD based actuator disc technique compared to detailed measurement,” *Int. J. Renew. Energy Dev.*, vol. 4, no. 3, pp. 205–210, 2015, doi: 10.14710/ijred.4.3.205-210.
- [9] U. Ali, M. Modrek, M. Islam, and I. Janajreh, “numerical study of airfoil shape and blade pitching on vertical axis wind turbine through cfd simulations,” *ASME Int. Mech. Eng. Congr. Expo. Proc.*, vol. 8, pp. 1–8, 2020, doi: 10.1115/IMECE2020-24003.
- [10] ANSYS FLUENT 13 User’s Guide, “Ansys Fluent Theory Guide,” *ANSYS Inc., USA*, vol. 15317, no. November, pp. 724–746, 2013.
- [11] J. Riglin and B. Reid, *Applied Computational Fluid Dynamics and Turbulence Modeling*, vol. 59, no. 5, 2021.
- [12] T. Manual, “Ansys Icem Cfd 11.0,” no. January, 2007.
- [13] “Centro de Investigaciones Energéticas, Medioambientales Tecnológicas (CIEMAT),” 2010. <https://www.ciemat.es/>.
- [14] C. E. Carcangiu, “CFD-RANS Study of Horizontal Axis Wind Turbines Thesis for the degree of Doctor of Philosophy,” *Meccanica*, no. January, p. 141, 2008, [Online]. Available: <http://veprints.unica.it/84/>.